


Incoherent Active Convolved Illumination Enhances the Signal-to-Noise Ratio for Shot Noise: Experimental Evidence

Wyatt Adams^{1,2}, Anindya Ghoshroy^{1,3} and Durdu Ö. Güney^{1,*}

¹*Department of Electrical and Computer Engineering, Michigan Technological University, 1400 Townsend Drive, Houghton, Michigan 49931-1295, USA*

²*Ansys, Inc., 2600 Ansys Drive, Canonsburg, Pennsylvania 15317, USA*

³*Caltech Optical Imaging Laboratory, Andrew and Peggy Cherng Department of Medical Engineering and Department of Electrical Engineering, California Institute of Technology, 1200 E. California Blvd., Pasadena, California 91125, USA*

 (Received 4 April 2022; revised 23 November 2022; accepted 2 December 2022; published 26 December 2022)

Imaging is indispensable for nearly every field of science, engineering, technology, and medicine. However, measurement noise and stochastic distortions pose fundamental limits to accessible spatiotemporal information despite impressive tools such as structured-illumination microscopy (SIM), stochastic optical reconstruction microscopy or photoactivated localization microscopy (STORM or PALM), and stimulated-emission-depletion (STED) microscopy. How to combat this challenge ideally has been an open question for decades. Inspired by a *virtual-gain* technique to compensate losses in metamaterials, *active convolved illumination* (ACI) has recently been proposed to significantly improve the signal-to-noise ratio and hence the data acquisition. In this technique, the light pattern of the object is superimposed with a correlated auxiliary pattern, the function of which is to reverse the adverse effects of losses, noise, and random distortion based on their spectral characteristics. Despite enormous implications in statistics, any experimental evidence verifying the theory of this novel technique has been lacking to date. We find experimentally that ACI boosts not just the resolution limit and image contrast but also the resistance to pixel saturation. The results confirm the previous theories and may open up horizons in a wide range of disciplines from atmospheric sciences, seismology, biology, statistical learning, finance, and information processing to quantum noise beyond the fundamental boundaries.

DOI: [10.1103/PhysRevApplied.18.064080](https://doi.org/10.1103/PhysRevApplied.18.064080)

I. INTRODUCTION

Imaging is an indispensable tool in the toolbox of nearly every field of science, engineering, technology, and medicine. Unfortunately, encoding the desired information into electromagnetic waves imposes a limit to the performance of imaging systems at the outset—the detection of the fields by the interaction of photons (the light signal) and matter (the light detector) means that the signal-to-noise ratio (SNR) for long exposures will always be limited physically by shot noise. A naive analysis would reveal that adding up more photons in the detector would lead to a higher SNR. This is true; however, typically (e.g., for incoherent light), the magnitude of the transfer function for an imaging system with an unobstructed pupil decreases with increasing spatial frequency [1]. It follows that the spectral SNR then also decreases with increasing spatial frequency, since the shot-noise variance is constant in the spatial-frequency domain [2–4]. Consequently, adding up

more photons blindly does not lead to much increase for the SNR of high spatial frequencies. One also does not have the freedom to arbitrarily increase the number of photons collected, since at some point the detector will become saturated. Each specific imaging modality will have its specific limitations. For example, in fluorescence imaging, only a certain exposure can be obtained before photo-bleaching occurs and high intensity becomes detrimental for live specimens.

Subwavelength optical engineering through metamaterials and metasurfaces offers unprecedented opportunities in a wide range of applications such as superresolution imaging [5–9], photolithography [10,11], wireless and optical communications [12,13], multifunctional and flat optics and photonics [14–16], metalenses [17], intelligent metaphotonics [18], light detection and ranging [19], autonomous vehicles [20], and quantum information [21,22]. However, the photon losses hinder their further viability [23–25]. Inspiration from research in loss compensation for metamaterials and plasmonics employing *virtual gain* [25–28] leads us to propose a perspective

*Corresponding author. dgüney@mtu.edu

on the noisy imaging problem [2,27,29–34]. The fundamental resolution limit to superresolving lenses is not determined by the diffraction limit but, rather, by a shot-noise limit, i.e., where the shot noise overcomes the transfer function in the spatial-frequency domain [4,35–37]. How to tackle this problem ideally has been an open question for decades [36–40]. The *active convolved illumination* (ACI) technique has recently been proposed theoretically as a ubiquitous noise and distortion mitigation scheme to improve the image SNR by systematically manipulating the image spectrum depending on the underlying stochastic behavior [2,27,31–34]. Popular techniques to improve the image resolution or the SNR are structured-illumination microscopy (SIM) [3,41–44], stimulated-emission-depletion (STED) microscopy [41,45,46], stochastic optical reconstruction microscopy or photoactivated localization microscopy (STORM or PALM) [41,47,48], and computational methods [36–40, 49,50] including machine learning [35,51]. An interesting method for far-field imaging with a constant *photon budget* (i.e., a constant number of photons in the object plane), based on a split-pupil optimization, has recently been put forward to break the SNR limit imposed by Fermat’s principle [4]. However, ACI operates down at the physical layer and enhances data acquisition; thus it is expected to benefit both conventional and novel approaches.

The working principle of the ACI technique is illustrated in Fig. 1. As shown in Fig. 1(a), most imaging systems suffer from various mechanisms of signal photon loss, such as impedance mismatch, absorption, scattering, diffraction, and noise. This, in general, results in a low-fidelity information transfer from the object plane to the receiver plane. It has been hypothesized that the ACI could overcome the loss of information as depicted in Fig. 1(b) [2,27,31,32]. The light pattern that forms the object (black line) is superimposed with an auxiliary pattern (blue line) correlated with the object. Therefore, the light pattern on the same object plane differs from the object. The purpose of the auxiliary is to manipulate the image spectrum to compensate the adversary photons, so that the object pattern is transferred through the system unscathed. The auxiliary pattern is typically found by characterizing the spectral distribution of noise obtained from the reference imaging system in Fig. 1(a) [2], as the noise poses the fundamental limit to accessible spatial information [4,35,36]. The auxiliary and object patterns can also be implemented as an inherently single entity (i.e., from a single undivided source) in the object plane, as shown in Fig. 1(c) [33]. Negative values for the auxiliary are not precluded. For incoherent imaging, this physically means that the energy is reduced at those locations, which is indeed useful to prevent excessive noise, long average exposure, and pixel saturation. Another equivalent implementation, which is discussed

theoretically and realized experimentally in the present work, is illustrated in Fig. 1(d). In contrast with Figs. 1(b) and 1(c), where the image spectrum is manipulated from the object plane only, here, instead, it is manipulated from both the object plane, via a varied exposure time or intensity, and the pupil plane simultaneously. Utilizing the pupil plane aids in a simple construction of an embedded auxiliary (i.e., embedded with the original object pattern as a single entity) in the object plane. In this case, the embedded auxiliary is simply proportional to the original object pattern.

The previous works on the foundations of ACI [2,27,31–34], along with further inspiration from other research on noisy far-field imaging [3,4], lead us to construct the current work. Following the implementation sketched in Fig. 1(d), we find for incoherent light that by suppressing the detection of the high-SNR spatial-frequency harmonics in an object, while amplifying the magnitude of those with a low SNR, the resulting image can have a large SNR for previously low-SNR spatial frequencies, due to prudent control of the flat overall noise level dictated by the Poisson distribution. This not only manages the exposure time efficiently but also leads to enhanced image resolution and contrast beyond what is possible with common postprocessing.

The previous body of literature [2,27,31–34] on ACI has been only theoretical and has typically utilized a high-spatial-frequency pass-band function, in conjunction with an increased exposure, to enhance the resolution performance of thin metal films acting as near-field plasmonic superlenses [2,31–34]. This pass-band function has been used not only to compensate the losses inherent in the metal film (i.e., virtual gain) but also to improve the image-spectrum SNR, similar to what we show in this work at far field. This imaging method has been called [32] “active convolved illumination” for a couple of reasons. First, the term “active” has been chosen since an added energy [33] (though not strictly necessary) has been used to obtain enhancement over the control (a bare superlens). Second, the term “convolved” has been chosen since the applied pass-band function is physically convolved with the fields emanating from the object. For coherent illumination, this pass-band function can be realized by a hyperbolic metamaterial (HMM) [33,34]. While there is no Fourier plane in the near-field configuration, the HMM can modify the Fourier components of the incident evanescent waves by its dispersion. In this case, the pupil function can then simply be thought of as the coherent transfer function of the cascaded HMM-superlens system and the SNR for the large spatial frequencies is enhanced with respect to the control.

Below, first a theory of ACI for incoherent light is presented that shows how to improve the SNR for the high spatial frequencies (i.e., the low-SNR components)

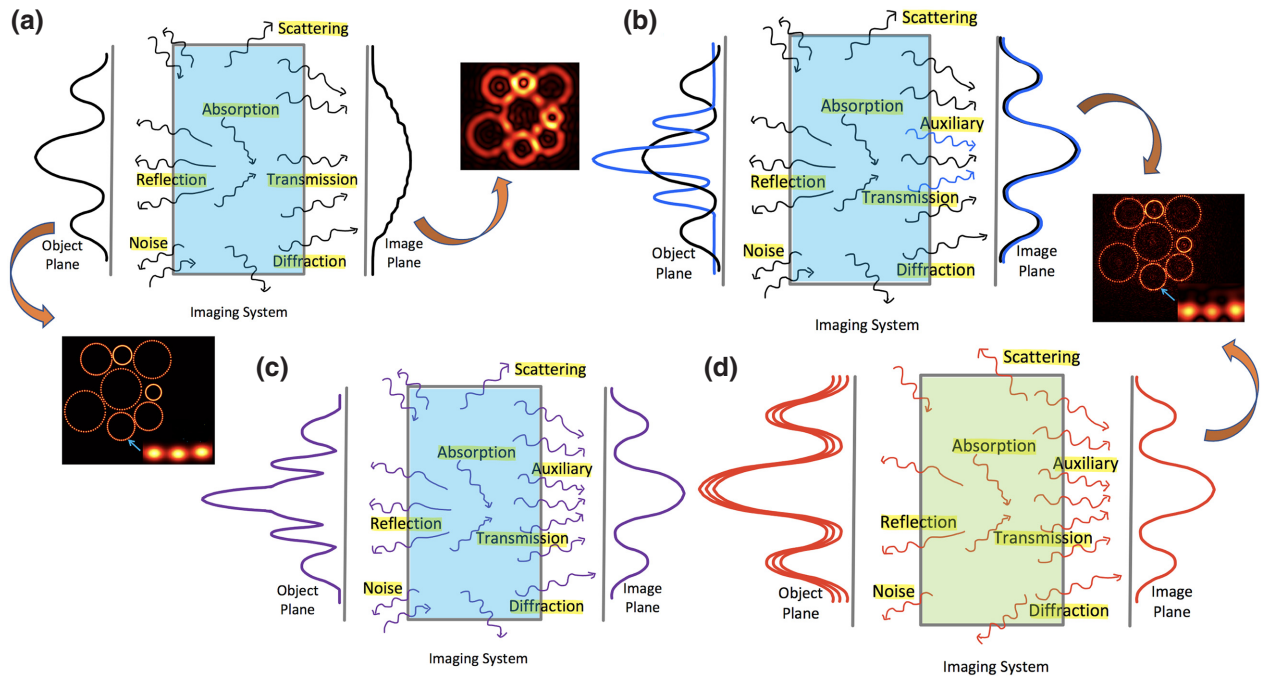


FIG. 1. The working principle of the ACI technique. (a) Most imaging systems suffer from loss of information due to physical processes such as reflection, absorption, scattering, diffraction, and noise. This results in an image with poor resolution and contrast. (b) In the ACI technique, the light pattern forming the object (black line) is superimposed with an auxiliary pattern (blue line), the purpose of which is to compensate the adversary photons that cause the information leakage from the system. The auxiliary is correlated with the object and, typically, based on the underlying spectral noise distribution. The result is a remarkable acquisition of data and hence a high-fidelity image. (c),(d) Equivalent to (b) except that the auxiliary and object patterns are implemented as an inherently single entity by utilizing (c) the object plane only or (d) both the object and pupil planes simultaneously instead. The implementation in (d) may lead to a greatly simplified embedded auxiliary in the object plane and hence a simple physical construction.

of an image obtained from an object illuminated with incoherent light. The theory is implemented in numerical simulations to predict the resolution enhancement and experimental images are collected using a low-numerical-aperture imaging system to confirm the predictions. The end result is an image with higher resolution and improved contrast as compared to the control image. It is also shown that ACI can help prevent pixel saturation for longer exposures. The experimental work here confirms that the theories of ACI are, in fact, both consistent with real noisy optical signals and can be extended to conventional far-field imaging systems and potentially to complex systems with different noise and distortion characteristics. A detailed understanding of random processes in the Fourier domain, crucial for the implementation of the ACI, and the subsequent development of the auxiliary pattern [Fig. 1(b)] or the equivalent combined light pattern for the object [Figs. 1(c) and 1(d)], immune to such distorting effects, may in general open up multiple avenues of research. It may lead to a generalized theory of randomly distorted systems pervading a wide range of disciplines from atmospheric sciences, seismology, finance, and biology to the mesoscopic physics of noisy quantum systems.

II. THEORETICAL MODEL

Let us consider a uniform beam of spatially incoherent narrow-band light with photon flux density (photons/ $m^2 s$) striking a planar transmissive object. After passing through the object, the light has spatial variations and the resulting transmitted photon flux density is given by $O(\mathbf{r})$, where $\mathbf{r} \in \mathbb{R}^2$ denotes the position coordinate on the plane. The process of mapping this light distribution with an imaging system can be represented by a convolution

$$I(\mathbf{r}) = H(\mathbf{r}) * O(\mathbf{r}), \quad (1)$$

where $I(\mathbf{r})$ is the photon flux density on the image plane, $H(\mathbf{r})$ is the unshifted point spread function (PSF) of the imaging system, and $*$ denotes the convolution. Here, it should be noted that $I(\mathbf{r}), O(\mathbf{r}) \in \mathbb{R}_{\geq 0}$, since they represent flux densities and not complex fields. Applying the convolution theorem and using the normalized image and object spectra, $\tilde{I}(\mathbf{k})$ and $\tilde{O}(\mathbf{k})$, respectively, Eq. (1) gives

$$\tilde{I}(\mathbf{k}) = \tilde{H}(\mathbf{k})\tilde{O}(\mathbf{k}), \quad (2)$$

where $\tilde{H}(\mathbf{k})$ is the optical transfer function (OTF) of the imaging system [1]. In general, $\tilde{I}(\mathbf{k}), \tilde{H}(\mathbf{k}), \tilde{O}(\mathbf{k}) \in \mathbb{C}$.

For later use, we define $|\tilde{H}(\mathbf{k})|$ as the modulation transfer function (MTF).

Equations (1) and (2) assume continuous signals in position and reciprocal space. To incorporate practical detection of the deterministic signal $I(\mathbf{r})$, let us consider the case where we collect an image on the image plane using a photoelectric detector with n_p pixels. The center of the p th pixel ($p \in \mathbb{Z}_+$) is at $\mathbf{r}_p = (x_i, y_j)$ and the pixels are rectangular with side lengths Δx and Δy along the x and y dimensions, respectively. Then, at the p th pixel, the expected number of detected photons is given by

$$\begin{aligned}\bar{I}_p &= \eta T \int_{A_p} I(\mathbf{r}) d^2\mathbf{r} \\ &= \eta T \int_{y_j - \Delta y/2}^{y_j + \Delta y/2} \int_{x_i - \Delta x/2}^{x_i + \Delta x/2} I(x, y) dx dy \\ &\approx \eta T \Delta x \Delta y I(x_i, y_j),\end{aligned}\quad (3)$$

where η is the quantum efficiency of the pixel and T is the exposure time or integration time. The approximation in the third line of Eq. (3) assumes that the signal $I(\mathbf{r})$ is slowly varying across the area of the pixel, i.e., the signal is well sampled. Since Eq. (3) describes a sampling of a spatial distribution of discrete particles (photons), there will be an intrinsic randomness due to shot noise in the photon signal $I_{p,\gamma}$. In this case, the probability mass function (PMF) is

$$\mathcal{P}(I_{p,\gamma} | \bar{I}_p) = \frac{(\bar{I}_p)^{I_{p,\gamma}}}{I_{p,\gamma}!} e^{-\bar{I}_p}.\quad (4)$$

This is, of course, coming from the fact that the counting of discrete particles at a constant rate follows a Poisson distribution, for which

$$\text{Var}(I_{p,\gamma}) = \bar{I}_p.\quad (5)$$

In most photoelectronic imaging detectors, such as complementary metal-oxide semiconductor (CMOS) or charge-coupled-device cameras, there are primarily two sources of noise. The first is due to the statistics of Eq. (4), the shot noise which is dependent on the photon signal. The second is noise from the readout electronics, which is independent of the photon signal. We can then write the detected signal as

$$I_p = \bar{I}_p + N_{p,\gamma} + N_{p,e},\quad (6)$$

where $N_{p,\gamma}$ is a discrete random variable representing the shot noise with PMF described by Eq. (4) and $N_{p,e}$ is a discrete random variable representing the electronic readout noise.

In order to show how the noise addition in Eq. (6) affects the image spectrum, we compute the discrete Fourier transform

$$\begin{aligned}\tilde{I}_q &= \sum_p I_p e^{-i2\pi \mathbf{k}_q \cdot \mathbf{r}_p} \\ &= \sum_p (\bar{I}_p + N_{p,\gamma} + N_{p,e}) e^{-i2\pi \mathbf{k}_q \cdot \mathbf{r}_p} \\ &= \sum_p \bar{I}_p e^{-i2\pi \mathbf{k}_q \cdot \mathbf{r}_p} + \sum_p N_{p,\gamma} e^{-i2\pi \mathbf{k}_q \cdot \mathbf{r}_p} \\ &\quad + \sum_p N_{p,e} e^{-i2\pi \mathbf{k}_q \cdot \mathbf{r}_p} \\ &= \tilde{I}_q + \tilde{N}_{q,\gamma} + \tilde{N}_{q,e},\end{aligned}\quad (7)$$

where $q \in \mathbb{Z}_+$ and $\{\mathbf{k}_q = (k_{x,l}, k_{y,m}) \mid 1 \leq q \leq n_p\} \subset \{\mathbf{k} \in \mathbb{R}^2\}$ is the Fourier space corresponding to the pixelated position space $\{\mathbf{r}_p \mid 1 \leq p \leq n_p\}$. We then consider the statistical properties of $\tilde{N}_{q,\gamma}$ and $\tilde{N}_{q,e}$. Since the shot-noise variance is known from Eq. (5) (replacing $I_{p,\gamma}$ with $N_{p,\gamma}$) and we can assume that the pixels are statistically independent, we can write [2–4]

$$\begin{aligned}\text{Var}(\tilde{N}_{q,\gamma}) &= \text{Var}\left(\sum_p N_{p,\gamma} e^{-i2\pi \mathbf{k}_q \cdot \mathbf{r}_p}\right) \\ &= \sum_p \text{Var}(N_{p,\gamma}) |e^{-i2\pi \mathbf{k}_q \cdot \mathbf{r}_p}|^2 \\ &= \sum_p \bar{I}_p = n_\gamma,\end{aligned}\quad (8)$$

where n_γ is the total expected number of photons in the entire image. In words, Eq. (8) states that the variance in Fourier space is constant and is controlled by the total expected number of photons collected on the detector. We can write a similar equation for the readout noise [3],

$$\begin{aligned}\text{Var}(\tilde{N}_{q,e}) &= \text{Var}\left(\sum_p N_{p,e} e^{-i2\pi \mathbf{k}_q \cdot \mathbf{r}_p}\right) \\ &= \sum_p \text{Var}(N_{p,e}) |e^{-i2\pi \mathbf{k}_q \cdot \mathbf{r}_p}|^2 = \sum_p \sigma_{p,e}^2,\end{aligned}\quad (9)$$

where $\sigma_{p,e}^2$ is the readout-noise variance at pixel p and again the assumption is made that the pixels are statistically independent. Let us also assume that $\sigma_{p,e}^2 = \sigma_e^2$, meaning that every pixel has similar electrical performance in terms of noise. Then Eq. (9) becomes

$$\text{Var}(\tilde{N}_{q,e}) = n_p \sigma_e^2.\quad (10)$$

Therefore, the spectral readout-noise variance is also a constant and scales linearly with the number of pixels.

For modern cameras, the readout noise is usually minimal such that it is neglected, though we keep it here for completeness.

From imaging theory, we know that the OTF of an incoherent imaging system is given by the normalized auto-correlation [1] of the pupil function $\tilde{P}(\mathbf{k})$ of the system, or

$$\tilde{H}(\mathbf{k}) = \frac{\int \tilde{P}(\boldsymbol{\kappa})\tilde{P}^*(\boldsymbol{\kappa} - \mathbf{k})d^2\boldsymbol{\kappa}}{\int |\tilde{P}(\boldsymbol{\kappa})|^2 d^2\boldsymbol{\kappa}}. \quad (11)$$

In the discrete notation described above, we can write

$$\tilde{H}_q = \frac{\sum_{\boldsymbol{\kappa}} \tilde{P}_{\boldsymbol{\kappa}}\tilde{P}_{\boldsymbol{\kappa}-\mathbf{k}_q}^*}{\sum_{\boldsymbol{\kappa}} |\tilde{P}_{\boldsymbol{\kappa},o}|^2} = \alpha \tilde{P}_q \star \tilde{P}_q, \quad (12)$$

where $\tilde{P}_{\boldsymbol{\kappa},o}$ is a reference pupil, α is the normalization constant, and \tilde{P}_q is the pupil function in the discrete notation. To normalize Eq. (12), the reference pupil is conventionally chosen as the pupil itself, making the dc pixel of $\tilde{H}_0 = 1$, similar to Eq. (11). However we define a reference pupil in Eq. (12) in order to later directly compare two different pupil functions. Consider an incoherent imaging system in air with maximum resolvable spatial frequency $k_{\max} = 2\text{NA}k_0$, where NA is the numerical aperture, $k_0 = 1/\lambda_0$, and λ_0 is the center free-space wavelength of the illumination source. The pupil function is assumed to have circular symmetry about the optical axis (which is along the z direction) and we define it as

$$\tilde{P}_q = \begin{cases} 1, & \text{if } k_- \leq |\mathbf{k}_q| \leq k_+, \\ 0, & \text{otherwise,} \end{cases} \quad (13)$$

where $k_- \geq 0$ and $k_- < k_+ \leq k_{\max}/2$. From Eq. (13), we can see that setting $k_- = 0$ and $k_+ = k_{\max}/2$ gives a typical diffraction-limited imaging system with an open pupil. We choose this case as our reference pupil $\tilde{P}_{q,o}$. However, if we make k_- nonzero, we introduce an obstruction in the central portion of the pupil, which has the effect of lowering the overall transmission with respect to the reference pupil and also preferentially reinforcing larger spatial frequencies with respect to the smaller ones in comparison to the reference pupil.

An important metric for an imaging system is its ability to discern image-spectrum content from noise, or its spectral SNR. To relate the pupil function to the spectral SNR, we first use Eqs. (2) and (12), without normalization, to rewrite the expected image spectrum as

$$\tilde{I}_q = [\beta \tilde{P}_q \star \tilde{P}_q] \tilde{O}_q = \tilde{\mathcal{H}}_q \tilde{O}_q, \quad (14)$$

where $\beta \tilde{P}_q \star \tilde{P}_q = \tilde{\mathcal{H}}_q$ is the unnormalized OTF and β is a new constant. Using a standard definition of SNR, we then

can write

$$\begin{aligned} \text{SNR}_q &= \frac{|\tilde{I}_q|}{\sqrt{n_\gamma + n_p \sigma_e^2}} = \frac{|\beta \tilde{P}_q \star \tilde{P}_q| \tilde{O}_q}{\sqrt{n_\gamma + n_p \sigma_e^2}} \\ &= \frac{|\tilde{\mathcal{H}}_q \tilde{O}_q|}{\sqrt{n_\gamma + n_p \sigma_e^2}} \end{aligned} \quad (15)$$

as the image-spectrum SNR. In Eq. (15), the numerator is the expected image spectrum, which can be engineered by manipulation of the pupil function, and the denominator is the total standard deviation of the signal from the photonic and electronic noise terms in Eqs. (8) and (9). An obvious consequence of Eq. (15) is that reducing n_γ will decrease the constant noise floor in the image spectrum. The signal in the numerator will also decrease similarly but can be engineered through \tilde{P}_q to enhance different portions of the spectrum. Conversely, increasing n_γ will increase the constant noise floor but this will also increase the signal. If the readout noise is neglected in Eq. (15), SNR_q will then theoretically increase with \sqrt{T} [Eq. (3)]. Interestingly, if one can additionally manipulate the pupil function to amplify certain spectral regions, further improvement in SNR_q becomes possible in those regions beyond the original shot-noise-limited signal. Engineering the system to preferentially pass a certain band or bands of the image spectrum while keeping the overall noise unchanged can also improve SNR_q for the selected regions. To put the latter scenario into analogy, we are given a *photobudget* (i.e., a constant number of photons in the image plane) [52] n_γ and we can freely decide how to spend that budget in the image spectrum via \tilde{P}_q so that we achieve an improved SNR for certain spatial frequencies. Boosting SNR with such spectrum-manipulation scenarios above considering the underlying noise statistics forms the essence of ACI and is the central theme of this work. The relation of these processes with the auxiliary pattern in Figs. 1(b) and 1(c) can be explained as follows.

Let $\tilde{\mathcal{H}}_{q,o}$ and $\tilde{\mathcal{H}}_{q,A}$ be the unnormalized OTFs for the imaging systems without (i.e., reference) and with ACI, respectively. Then, the expected image spectrum obtained by the auxiliary component becomes

$$\begin{aligned} \tilde{I}_{q,\text{aux}} &= \tilde{\mathcal{H}}_{q,A} \tilde{O}_q - \tilde{\mathcal{H}}_{q,o} \tilde{O}_q = \tilde{h}_q \tilde{\mathcal{H}}_{q,o} \tilde{O}_q - \tilde{\mathcal{H}}_{q,o} \tilde{O}_q \\ &= \tilde{\mathcal{H}}_{q,o} (\tilde{h}_q - 1) \tilde{O}_q, \end{aligned} \quad (16)$$

where we define the virtual gain $\tilde{h}_q = \tilde{\mathcal{H}}_{q,A}/\tilde{\mathcal{H}}_{q,o}$ with $\tilde{\mathcal{H}}_{q,o} \neq 0$. Therefore, the auxiliary pattern spectrum corresponding to Fig. 1(b) and the combined object spectrum and embedded auxiliary corresponding to Fig. 1(c) can be,

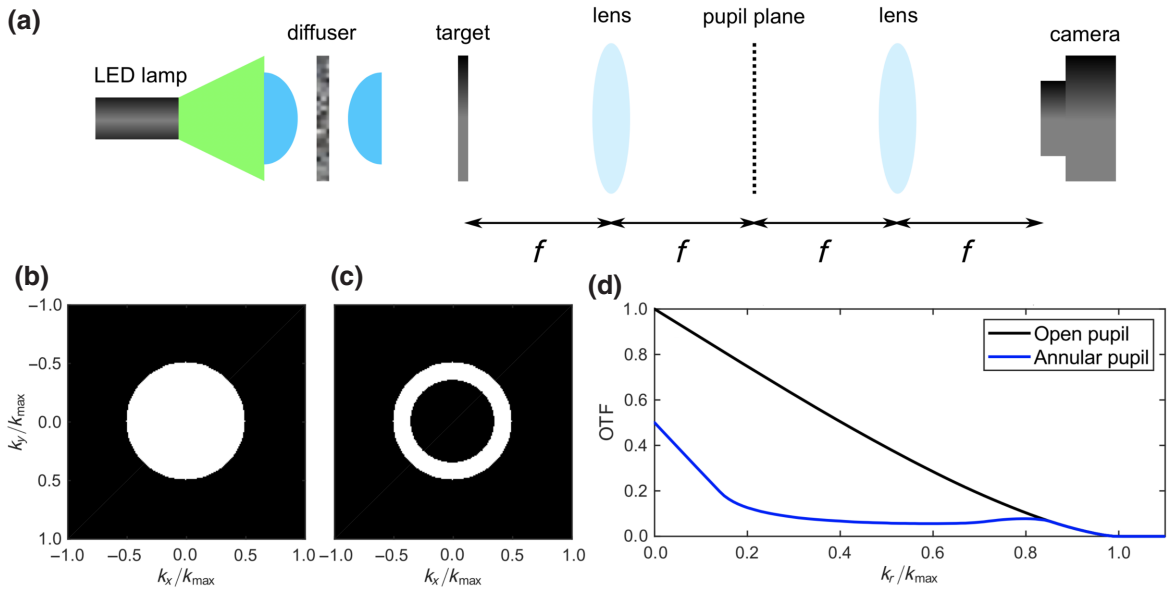


FIG. 2. The imaging-experiment configuration, the pupils used in the experiment, and the corresponding OTFs. (a) A diffused light-emitting diode (LED) source illuminates an imaging target, which is then processed by a $4f$ system consisting of two achromatic doublet lenses and a transparency in the pupil plane with a focal length of $f = 38.1$ cm. The images are detected with a CMOS camera. (b)–(d) Open (reference) (b) and annular (c) pupils with corresponding OTFs (d) calculated from Eq. (12) as a function of the radial spatial frequency $k_r = \sqrt{k_x^2 + k_y^2}$. Both pupils have $k_+ = k_{\max}/2$. In (b), $k_- = 0$ and in (c), $k_- = k_{\max}/2\sqrt{2}$. In the actual experiment, we choose an outer pupil diameter of 5 mm for (b) and (c), making $\text{NA} = 0.0066$. In (d), the OTF for the annular pupil is normalized with respect to open pupil to illustrate their relative transfer characteristics.

respectively, expressed as

$$\tilde{O}_{q,\text{aux}} = (\tilde{h}_q - 1)\tilde{O}_q, \quad (17)$$

$$\tilde{O}_{q,A} = \tilde{h}_q \tilde{O}_q, \quad (18)$$

which are both correlated with the object. $\tilde{\mathcal{H}}_{q,A}$ in Eq. (16) is also known as the *active transfer function* (ATF) [2] and proportional to the exposure time. If the ATF leads to amplification at some spatial frequencies with respect to the reference system, this implies virtual gain in that spectral region.

Similarly, to express the embedded auxiliary spectrum $\tilde{O}_{q,\text{aux}}$ of Fig. 1(d), we start with the transformation equation for the expected image spectrum

$$\tilde{I}_q = \tilde{H}_{q,a}(\tilde{O}_q + \tilde{O}_{q,\text{aux}}) = \tilde{H}_{q,A}\tilde{O}_q, \quad (19)$$

where $\tilde{H}_{q,a}$ is the unnormalized OTF of the imaging system in Fig. 1(d) when the exposure time is kept the same as the reference [Fig. 1(a)]. Then, we find

$$\tilde{O}_{q,\text{aux}} = (\tau - 1)\tilde{O}_q \quad (20)$$

where $\tau = \tilde{H}_{q,A}/\tilde{H}_{q,a}$ is the virtual gain for this system, which simply turns out to be the factor of increase in exposure time. Since both systems [Figs. 1(c) and 1(d)]

are designed to produce the same expected image spectrum $\tilde{H}_{q,A}\tilde{O}_q$, the spectral noise variance is also the same [Eq. (8)]. Therefore, both implementations equivalently manipulate the image spectrum using different auxiliaries. Needless to say, the intensity plays a role similar to that of the exposure time and we primarily consider the latter in our analysis. As described in Sec. III, the ACI in this work [Fig. 1(d)] is experimentally realized with the modified pupil (i.e., via $\tilde{H}_{q,a}$ in Eq. (19)) and the simple embedded auxiliary in Eq. (20).

III. EXPERIMENT

In order to implement the above spectral SNR manipulation in an experimental imaging system, we simply need access to the Fourier space in order to manipulate the pupil function. Therefore, we choose to construct a typical $4f$ system with no magnification, as shown in Fig. 2(a), in order to simplify the analysis and experiment.

The experimental setup in Fig. 2(a) images an object (target) illuminated by a narrow-band incoherent light source (Thorlabs LIU525B) at 525-nm wavelength. Before hitting the target, the light is focused onto a diffuser in order to decrease the spatial coherence and to avoid imaging the light source onto the pupil plane. Then the light is roughly collimated by a second lens before hitting the

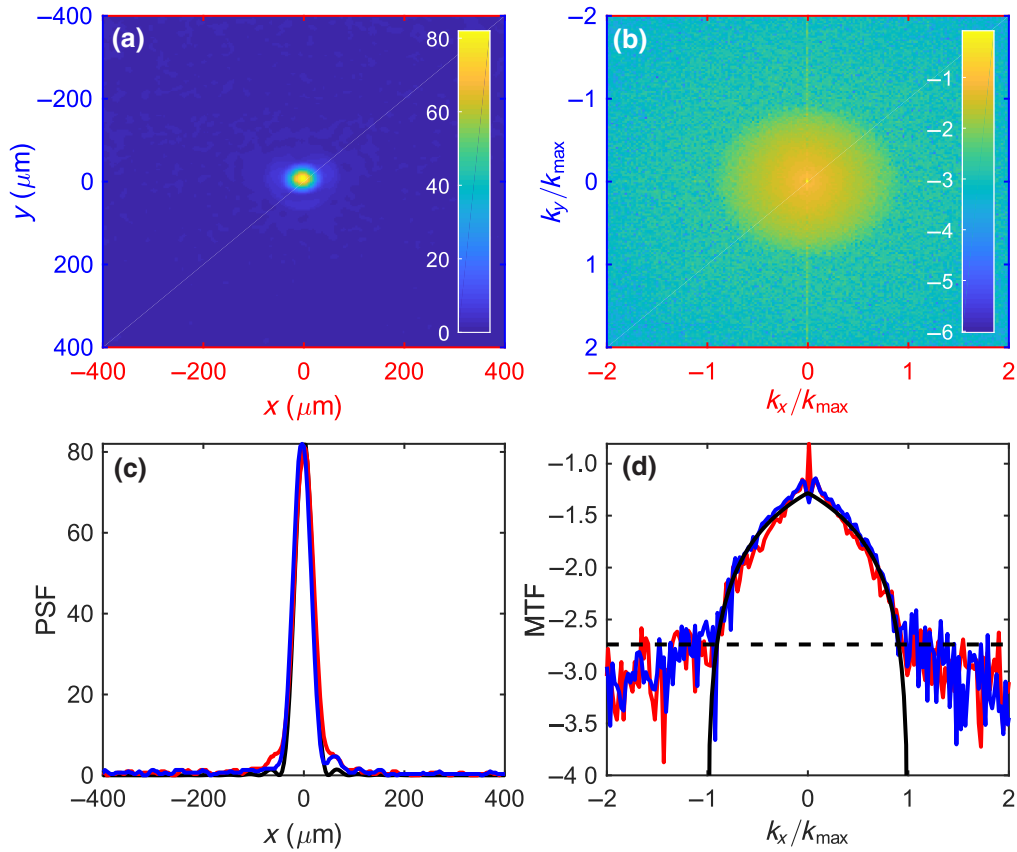


FIG. 3. The measured PSF and MTF for a full unobstructed pupil with $\text{NA} = 0.0066$ and an exposure time of $T = 2$ s. (a) The PSF collected from the setup in Fig. 2. (b) The MTF calculated by fast Fourier transformation of (a) in log scale. (c) Cross sections of (a) through the origin along x (red line) and y (blue line). The theoretical prediction is given by the black line. (d) Cross sections of (b) through the origin along k_x (red line) and k_y (blue line). The theoretical prediction is given by the solid black line. The dashed black line denotes the calculated shot-noise standard deviation using Eq. (8).

target. The light distribution exiting the target is transferred through an achromatic doublet lens (Space Optics Research Labs) with a focal length of $f = 38.1$ cm. On the pupil plane, a pupil transparency is placed that has either a circular or annular opening, as shown in Figs. 2(b) and 2(c). For all the images, we choose an outer-pupil diameter of $d = 5$ mm, making $\text{NA} = 0.0066$ using the formula $\text{NA} = d/2f$. The transparencies are printed with a photoplotter onto transparent plastic sheets, then cut out and mounted in standard optical mounts. After passing through the pupil plane, the light is again transferred through a second identical achromatic doublet, which then focuses the resulting image onto a CMOS camera (Thorlabs DCC1645C).

The goal of this experiment is to show directly an enhancement in image resolution by modifying the pupil and exposure time to improve SNR_q for the largest spatial frequencies, in accordance with Eq. (15). This leads to an annular-pupil configuration. The ACI here is then simply implemented with an annular pupil and variable photon exposure and the reference system with an open

pupil, using incoherent light at 525-nm wavelength [Figs. 2(b) and 2(c)]. The relative transfer characteristics of the open and annular pupils are plotted in Fig. 2(d). However, it should be emphasized that the concepts presented should be generally applicable to any imaging system that is linear and shift-invariant, provided that there is a mechanism with which to manipulate the Fourier content of the light.

To show quantitatively the improvement in the resolution performance afforded by the annular-pupil configuration with modified exposure over the open pupil, we replace the resolution target with a $10\text{-}\mu\text{m}$ -diameter pinhole. Since this diameter is below the diffraction limit for the chosen numerical aperture defined by k_+ and f , the resulting image of the pinhole gives the unshifted PSF of the imaging system at an arbitrary scale. These PSF images are taken with both the open- and annular-pupil transparencies, with varying exposure times. From these images, the OTFs and corresponding SNR_q can be computed for each exposure. It should be emphasized that in the present implementation, the annular pupil performs the first iteration of image-spectrum manipulation by accentuating

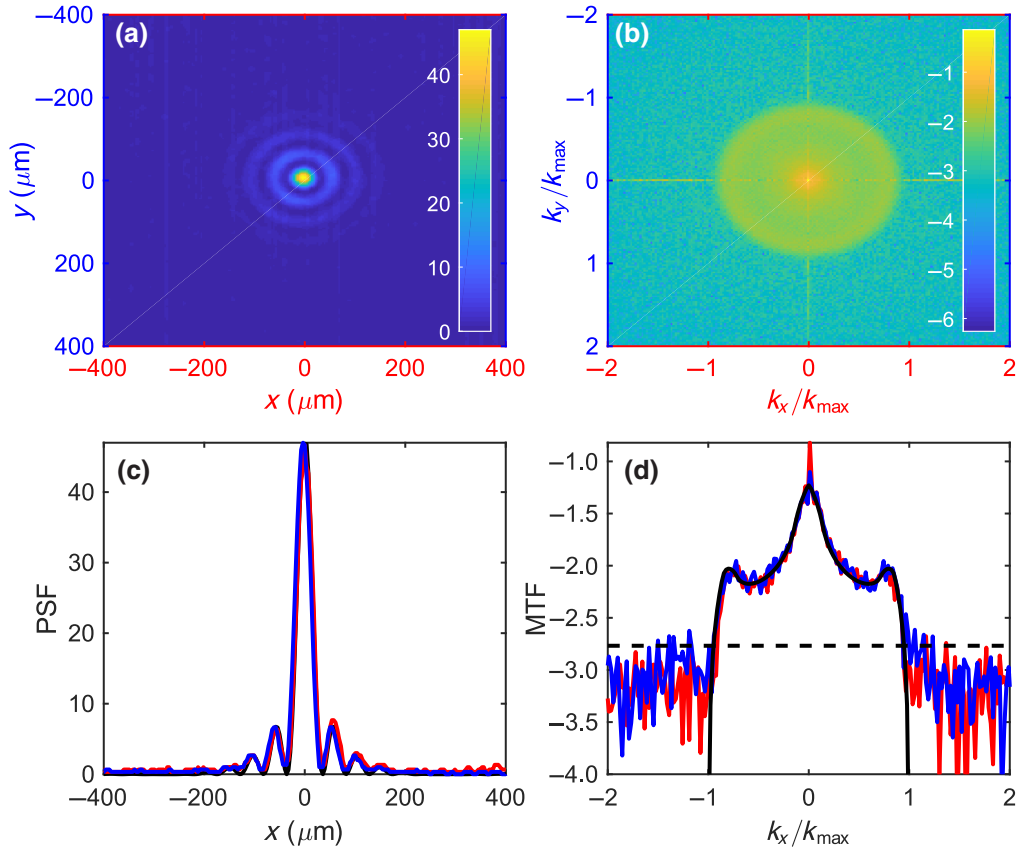


FIG. 4. The measured PSF and MTF for an annular pupil with $k_- = k_{\max}/2\sqrt{2}$, $\text{NA} = 0.0066$, and an exposure time of $T = 4$ s. The subfigures are defined in the same manner as in Fig. 3.

certain spatial frequencies, whereas the exposure time controls the necessary level of signal amplification or attenuation to transfer the right amount of auxiliary contribution to the image plane. The annular pupil with varied photon exposure, in effect, directly produces the required auxiliary [Eq. (20)] of the object plane as minted into the compound object-auxiliary pattern proportional to the exposure time. The level of exposure and the annular-pupil dimensions are determined carefully from the limiting spatial frequency of the reference system and the fact that *the shot-noise variance is constant and equal to the total expected number of photons* [Eq. (8)].

Examples of the experimentally measured PSFs and MTFs, with the same scaling factor as the PSFs, are presented in Figs. 3 and 4 for the open and annular pupils, respectively. Also shown are the theoretical PSFs and MTFs determined from scalar diffraction theory. Good agreement can be seen with both the PSF and MTF between theory (black lines) and experiment (red and blue lines), indicating that the imaging system is well aligned and not inducing any unwanted aberrations. Also, the calculated standard deviation (black dashed line) seems to accurately predict where the MTF signal is overcome by the shot noise, providing evidence supporting the

theoretical model for spectral noise. Since $\sigma_e = 0$ in this calculation, it is apparent that the readout noise is in fact likely negligible.

From the OTFs computed from the measured PSFs in Figs. 3 and 4, it is then straightforward to compute SNR_q for each exposure using Eq. (15), assuming that the experimental pixel values and the number of photons at each pixel are about linearly related. These are plotted in Fig. 5(a), where the solid lines indicate the open pupil SNR_q and the dashed lines indicate the annular pupil SNR_q . For a direct comparison of the SNR_q for the two pupil configurations, we define a spectral SNR improvement metric

$$\text{SNRi}_q = \frac{\text{SNR}_{q,a,T}}{\text{SNR}_{q,o,T_0}}, \quad (21)$$

where $\text{SNR}_{q,a,T}$ is the annular-pupil spectral SNR for exposure time T and SNR_{q,o,T_0} is the open-pupil spectral SNR for exposure time T_0 . Plotted in Fig. 5(b) is the SNRi_q for $T_0 = 2$ s and three different values of T . It can be seen that a clear enhancement in the SNR for spatial frequencies near $0.83k_{\max}$ can be obtained using an annular pupil provided that there is sufficient exposure.

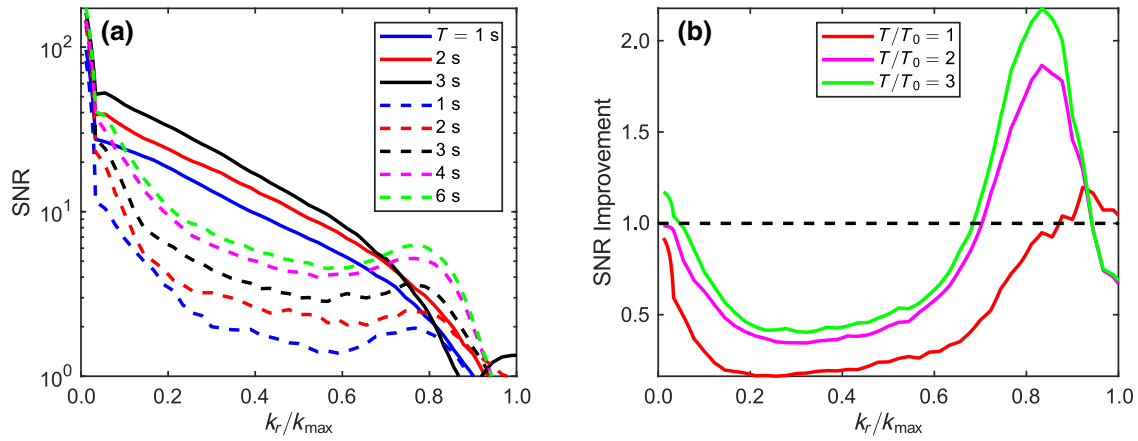


FIG. 5. The improvement in the spectral SNR. (a) The measured spectral SNR for open (solid lines) and annular (dashed lines) pupils for different exposure times. The crossover by the black solid line over the red and blue lines is due to distortion of the PSF by pixel saturation at $T = 3$ s for the open pupil. (b) The spectral SNR improvement SNR_i_q corresponding to the data in (a) with $T_0 = 2$ s. The black dashed line indicates $\text{SNR}_i_q = 1$.

To verify that the high-spatial-frequency improvement in spectral SNR with sufficient exposure manifests as improved image resolution, we image a USAF-1951 resolution test target (Thorlabs R1DS1N) using the setup in Fig. 2(a). The collected images for the open and annular pupils are shown in Fig. 6 for different values of T . Also shown are the corresponding reconstructions obtained by deconvolving the raw images with the Richardson-Lucy algorithm [39,40] after 30 iterations as implemented in MATLAB. In Figs. 6(a)–6(c), it can be seen that the three-bar target in element 5 is always blurred together by the open pupil (red solid rectangles); however, even for low exposure (e.g., $T = 10$ ms), the bars become qualitatively visible in the annular-pupil case (yellow solid rectangles). After reconstruction for 30 iterations, element 5 remains unresolved in the open-pupil images (red dashed rectangles) but the annular-pupil images of element 5 are further improved (yellow dashed rectangles).

When the exposure time T is increased, the spectral SNR for the experimental MTF (Figs. 3 and 4) is scaled by a factor of \sqrt{T} [Eqs. (3) and (15)] as long as no pixel saturation takes place. In particular, as shown in Fig. 5, the annular pupil selectively amplifies the amplitudes of the spatial frequencies within a specific range and improves the spectral SNR in that region even beyond the point that may not be otherwise possible due to the pixel saturation with the open pupil (i.e., the reference system). This enhancement may occur at the expense of a reduced spectral SNR in the other regions (e.g., lower spatial frequencies). However, those regions may be recovered easily with deconvolution. Particularly for elements 2–4 in Figs. 6(a)–6(c), the annular-pupil image is improved greatly by the reconstruction, since those spatial frequencies were originally attenuated with respect to the open pupil. Importantly, since the spectral noise variance is equal to the

total expected number of photons in the entire image [Eq. (8)], it is indeed advantageous to suppress the energy-rich regions so that the selective amplification successfully delivers power to the most demanding spectral band without (excessively) amplifying the noise. As a result, such a noise-behavior-driven spectrum manipulation, critical to the implementation of the ACI, enables us to push the SNR limit for the reference imaging system and significantly enhance the overall image contrast and resolution, as can be clearly seen in Figs. 6(a)–6(c). The improvement is prominent if, for instance, element 5 (both the raw and deconvolved images) obtained from the open pupil with $T = 10$ ms is compared with that of the annular pupil with $T = 50$ ms. Conversely, if element 5 obtained from the open pupil with $T = 50$ ms is compared with that of the annular pupil with $T = 10$ ms, it is also observed that the ACI can achieve higher resolution and contrast with shorter exposure—a highly desirable feature for bioimaging modalities to avoid photodamage [42–44,46,47,53] to the sample or eye-safe operations.

Next, in Fig. 6(d), we delve into an extreme case of photon exposure whereupon pixel saturation occurs. Upon viewing the open pupil SNR_q from Eqs. (3) and (15), nonetheless, it would seem that simply increasing T would lead to an improvement in SNR_q itself, without having to modify the pupil. However, the pixels in typical digital cameras only have a finite well depth and dynamic range, meaning that they can experience saturation for long exposures and/or intense illumination. The saturation causes a nonlinear response of the pixel as a function of the input photon signal. Therefore, one cannot arbitrarily increase T or the illumination intensity to increase SNR_q . In terms of spatial resolution, saturation can manifest as an effective blurring due to clipping of the pixel values and blooming of photoelectrons to adjacent pixels.

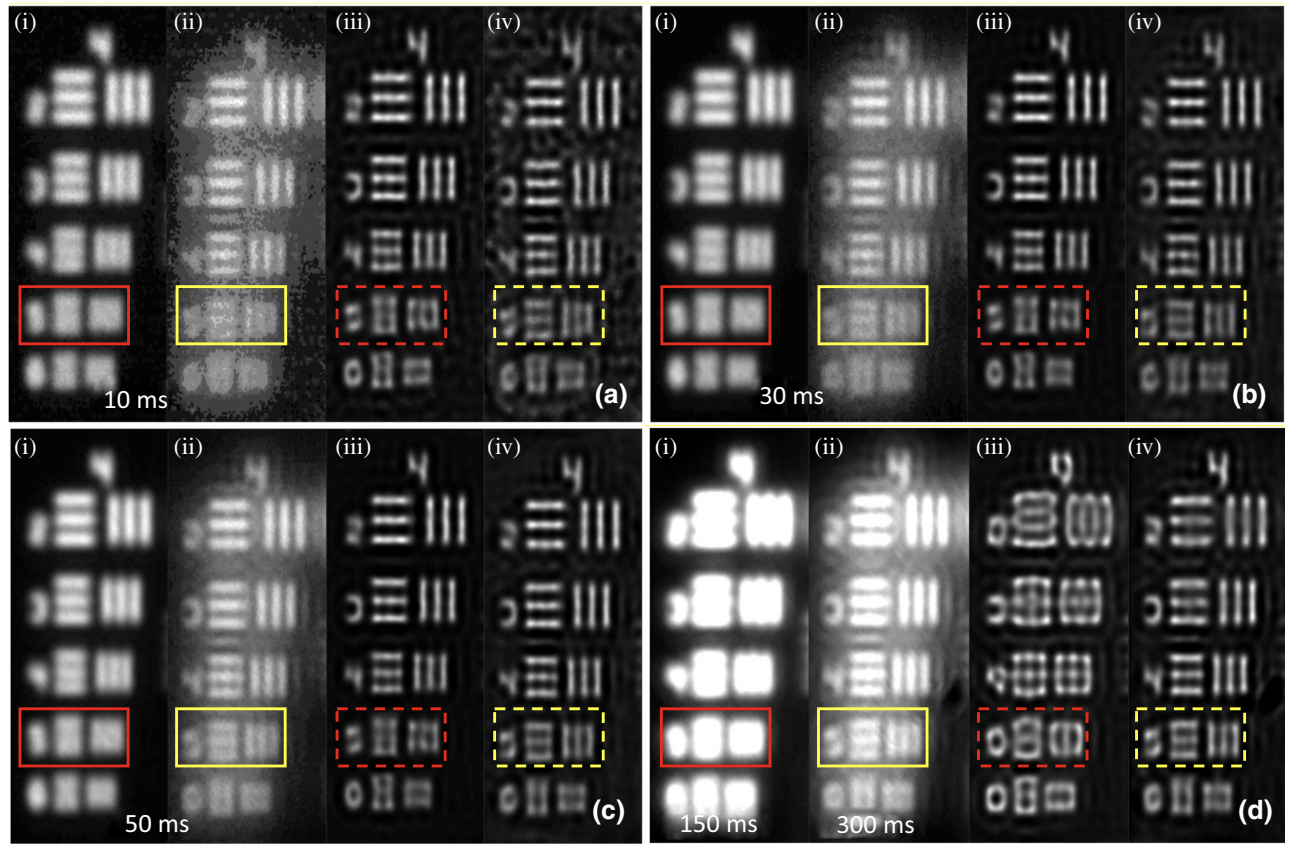


FIG. 6. Experimental images of a USAF-1951 resolution test target collected from the setup in Fig. 2: (a) $T = 10$ -ms, (b) $T = 30$ -ms, and (c) $T = 50$ -ms exposure times. The individual images in each subfigure correspond to the following: (i) a raw image collected with an open pupil in the pupil plane and $NA=0.0066$; (ii) a raw image with an annular pupil in the pupil plane and the same NA as (i); (iii) an image from (i) deconvolved by the Richardson-Lucy algorithm after 30 iterations; (iv) an image from (ii) deconvolved by the Richardson-Lucy algorithm after 30 iterations. The red rectangles highlight the raw (solid) and deconvolved (dashed) images for element 5 using the open pupil. Similarly, the yellow rectangles do so for the annular pupil. A clear improvement in image resolution and contrast is seen with the annular pupil. (d) Images demonstrating the resistance of the annular pupil to deleterious effects caused by detector saturation: (i)–(iv) and the rectangles are defined similarly to (a)–(c). For the open pupil, $T = 150$ ms, and for the annular pupil, $T = 300$ ms. It can be seen that even for a twice as long exposure time, the annular-pupil image quality is mostly maintained compared to the open-pupil image, which is severely blurred due to pixel saturation. The ACI is implemented with the annular pupil and varied photon exposure and the reference system with the open pupil.

Along with the provided improved resolution and contrast, the proposed spectrum-manipulation method can also provide resistance to pixel saturation in cases when long exposure or intense illumination *and* high resolution is required. To demonstrate this, we collect images in which the pixels become saturated for the open-pupil system and compared them to images in the annular-pupil system. They are shown in Fig. 6(d). Clearly, the annular pupil has higher resistance to pixel saturation than the open pupil, despite a twice-longer exposure time. Element 5 can never be resolved with the open pupil, as the pixel saturation appears earlier. A larger portion of the Fourier space is blocked by the annular pupil. As evidenced by Fig. 2(d), the blocked photons correspond to lower spatial frequencies, which are more likely to contribute to pixel saturation, since the transmission for these portions of the object will

be high due to the larger local photon flux. Therefore, a cleverly tuned selective amplification not only improves the resolution and contrast but also renders the imaging system more immune to the pixel saturation.

IV. DISCUSSION AND CONCLUSIONS

In this work, it is demonstrated experimentally that ACI enhances the SNR, image resolution, and contrast. This method utilizes manipulation of the Fourier space by employing an auxiliary, which both relies on the noise behavior and correlates with the object pattern, in order to tame the image-spectrum SNR. Here, this is simply achieved by an annular pupil and an embedded auxiliary with a variable exposure time. Placing an annular-pupil transparency in the pupil plane while adjusting the

photon exposure leads to an improved SNR for larger spatial frequencies, which gives improved resolution over an imaging system with an unobstructed pupil and the same numerical aperture. Also, the annular pupil increases resistance to pixel saturation, since a portion of the Fourier space is blocked and the number of photons at the detector is decreased. The theory and simulation of the proposed loss mitigation and resolution-enhancement method for incoherent light, the experiment to verify and expand upon the previous metamaterial implementations at near field [2,27,31–34], and how to manipulate the pupil or OTF of an imaging system to achieve a desired high-spatial-frequency SNR are discussed. The choice for the small NA in this proof-of-principle experiment is made mostly for practical reasons dictated by our bar target and achromatic doublet lenses. There is no theoretical limitation to applying this concept to a high-NA system such as a microscope objective. As long as there is access to the Fourier space, one can still modify the pupil function.

The spatial filtering properties of the annular pupil are well known and are commonly used in imaging systems [54]. However, the motivation in our work is different, in that we solely use the annular pupil to prove experimentally that the ACI concept, which has only been proposed theoretically so far, indeed works. To achieve that, we find one specific implementation that is mathematically equivalent to the previous theoretical implementations of the ACI. We choose the annular pupil with a controlled exposure time as a simple and convenient tool for this purpose. It is not our intention here to find an optimal or a unique implementation of the ACI, as this would require sophisticated spectral engineering (e.g., using machine learning and metaoptics) specifically optimized for the imaging system of interest with specific noise or distortion statistics. Instead, considering the implementation with the annular pupil and controlled exposure time as a simple example or case of ACI, our paper presents experimental evidence that the ACI idea is indeed well founded.

Similarly, spatial filtering with a central obscuration to block low spatial frequencies to achieve increased spectral SNR at higher spatial frequencies of the diffracted beam and avoid pixel saturation from the direct beam, such as in x-ray coherent diffraction imaging (CDI) [53], or for edge enhancement in different coherent imaging modalities may be regarded as a simple and special case of coherent ACI [2]. In general, more sophisticated use of ACI with clever illumination structuring [55] driven by the noise statistics [2] may deliver more favorable results in diverse imaging systems. For example, such a structured-illumination source immune to noise may improve the x-ray CDI measurements and the performance of reconstruction algorithms [56–58] by controlling the coherence of the incident illumination [58–60].

It is worth mentioning that the implementation of ACI presented here should not be confused with incoherent

edge detection, as the latter usually relies on bipolar incoherent image processing [61–63]. Also, although some of our methodologies are inspired by the recent split-pupil-optimization technique [4], the proposed technique here is more general, does not contend with a constant photon budget, and is intimately connected with the virtual-gain phenomenon in an earlier theoretical proposal [27], as illustrated schematically in Fig. 1(b). The ACI offers new opportunities for not only conventional imaging systems and superlenses but also various other linear systems. One can envision its potential generalization and ubiquity to encompass imaging through random media (e.g., turbulent and scattering atmosphere) [64–68], spectroscopy [69], \mathcal{PT} -symmetry [28,70,71], photolithography [10,11], and quantum information and image processing [72–74]. The virtual-gain mechanism employed in ACI can alleviate the stringent requirement of balance between loss and gain in \mathcal{PT} -symmetric systems [28]. It is important to note that the systems with more intricate noise or distortion characteristics (e.g., a turbulent atmosphere) may necessitate more ingenious engineering of the pupil function than here. Optimal and precise manipulation of the pupil function, beyond conventional optics, may be possible with the advent of amenable metasurfaces [14–16]. More work on ACI and potential relevance with SIM [3,41–44], superoscillatory imaging [74–77], and super-gain [78] can enrich further understanding of imaging beyond the known boundaries. Computational superresolution techniques [35–37,49,50] integrated with ACI enabled systems can provide extended resolution limits. Machine-learning approaches [35] bolstered with ACI may enable optical visualization of dynamic scenes at previously inaccessible scales. An interesting direction of research could be to utilize the analytical continuity principle [35–37] while enhancing the SNR with ACI to achieve far-field super-resolution imaging. Since ACI is fundamentally a physical process (i.e., physical preprocessing) that enhances speed, over time-consuming deconvolution, and data acquisition, it may benefit numerous imaging scenarios. It may also be possible to use cheap detectors and yet obtain the same imaging quality as that of expensive ones not aided by ACI.

ACKNOWLEDGMENTS

This work was supported by the Office of Naval Research (N00014-15-1-2684) and the National Science Foundation (EAR-2221730). We would like to thank Christopher Middlebrook at Michigan Technological University for fruitful discussions.

-
- [1] J. W. Goodman, *Introduction to Fourier Optics* (Roberts and Company Publishers, Englewood, CO, 2005).

- [2] A. Ghoshroy, W. Adams, and D. Ö. Güney, Theory of coherent active convolved illumination for superresolution enhancement, *J. Opt. Soc. Am. B* **37**, 2452 (2020).
- [3] E. A. Ingerman, R. A. London, R. Heintzmann, and M. G. L. Gustafsson, Signal, noise and resolution in linear and nonlinear structured-illumination microscopy, *J. Microsc.* **273**, 3 (2019).
- [4] J. Becker, R. Förster, and R. Heintzmann, Better than a lens—A novel concept to break the SNR-limit, given by Fermat's principle, [arXiv:1811.08267](https://arxiv.org/abs/1811.08267) [physics] (2018).
- [5] W. Adams, M. Sadatgol, and D. Ö. Güney, Review of near-field optics and superlenses for sub-diffraction-limited nano-imaging, *AIP Adv.* **6**, 100701 (2016).
- [6] J. L. Ponsetto, A. Bezryadina, F. Wei, K. Onishi, H. Shen, E. Huang, L. Ferrari, Q. Ma, Y. Zou, and Z. Liu, Experimental demonstration of localized plasmonic structured illumination microscopy, *ACS Nano* **11**, 5344 (2017).
- [7] Q. Ma, H. Hu, E. Huang, and Z. Liu, Super-resolution imaging by metamaterial-based compressive spatial-to-spectral transformation, *Nanoscale* **9**, 18268 (2017).
- [8] A. Bezryadina, J. Zhao, Y. Xia, X. Zhang, and Z. Liu, High spatiotemporal resolution imaging with localized plasmonic structured illumination microscopy, *ACS Nano* **12**, 8248 (2018).
- [9] Y. U. Lee, J. Zhao, Q. Ma, L. K. Khorashad, C. Posner, G. Li, G. Bimananda, M. Wisna, Z. Burns, J. Zhang, and Z. Liu, Metamaterial assisted illumination nanoscopy via random super-resolution speckles, *Nat. Commun.* **12**, 1559 (2021).
- [10] P. Gao, N. Yao, C. Wang, Z. Zhao, Y. Luo, Y. Wang, G. Gao, K. Liu, C. Zhao, and X. Luo, Enhancing aspect profile of half-pitch 32 nm and 22 nm lithography with plasmonic cavity lens, *Appl. Phys. Lett.* **106**, 093110 (2015).
- [11] G. Liang, X. Chen, Q. Zhao, and L. J. Guo, Achieving pattern uniformity in plasmonic lithography by spatial frequency selection, *Nanophotonics* **7**, 277 (2018).
- [12] L. Si, H. Jiang, and X. Lv, and J. Ding, Broadband extremely close-spaced 5G MIMO antenna with mutual coupling reduction using metamaterial-inspired superstrate, *Opt. Express* **27**, 3472 (2019).
- [13] W. Yang and Y.-S. Lin, Tunable metamaterial filter for optical communication in the terahertz frequency range, *Opt. Express* **28**, 17620 (2020).
- [14] Y. Zhou, I. I. Kravchenko, H. Wang, H. Zheng, G. Gu, and J. Valentine, Multifunctional metaoptics based on bilayer metasurfaces, *Light: Sci. Appl.* **8**, 80 (2019).
- [15] Y. Zhou, H. Zheng, I. I. Kravchenko, and J. Valentine, Flat optics for image differentiation, *Nat. Photonics* **14**, 316 (2020).
- [16] J. Rho, Metasurfaces: Subwavelength nanostructure arrays for ultrathin flat optics and photonics, *MRS Bulletin* **45**, 180 (2020).
- [17] S. Banerji, M. Meem, A. Majumder, F. Guevara Vasquez, B. Sensale-Rodriguez, and R. Menon, Imaging with flat optics: Metalenses or diffractive lenses?, *Optica* **6**, 805 (2019).
- [18] S. Krasikov, A. Tranter, A. Bogdanov, and Y. Kivshar, Intelligent metaphotonics empowered by machine learning, *Opto-Electron. Adv.* **5**, 210147 (2022).
- [19] A. C. Lesina, D. Goodwill, E. Bernier, L. Ramunno, and P. Berini, Tunable plasmonic metasurfaces for optical phased arrays, *IEEE J. Sel. Top. Quantum Electron.* **27**, 4700116 (2020).
- [20] R. Zecca, D. L. Marks, and D. R. Smith, Symphotic design of an edge detector for autonomous navigation, *IEEE Access* **7**, 144836 (2019).
- [21] S. A. Uriri, T. Tashima, X. Zhang, M. Asano, M. Bechu, D. Ö. Güney, T. Yamamoto, Ş. K. Özdemir, M. Wegener, and M. S. Tame, Active control of a plasmonic metamaterial for quantum state engineering, *Phys. Rev. A* **97**, 053810 (2018).
- [22] M. Mirhosseini, E. Kim, V. S. Ferreira, M. Kalae, A. Sipahigil, A. J. Keller, and O. Painter, Superconducting metamaterials for waveguide quantum electrodynamics, *Nat. Commun.* **9**, 3706 (2018).
- [23] J. B. Khurgin and G. Sun, In search of the elusive lossless metal, *Appl. Phys. Lett.* **96**, 181102 (2010).
- [24] A. Krasnok and A. Alù, Active nanophotonics, *Proc. IEEE* **108**, 628 (2020).
- [25] A. Ghoshroy, Ş. K. Özdemir, and D. Ö. Güney, Loss compensation in metamaterials and plasmonics with virtual gain, *Opt. Mater. Express* **10**, 1862 (2020).
- [26] E. O. Potma, C. Evans, X. S. Xie, R. J. Jones, and J. Ye, Picosecond-pulse amplification with an external passive optical cavity, *Opt. Lett.* **28**, 1835 (2003).
- [27] M. Sadatgol, Ş. K. Özdemir, L. Yang, and D. Ö. Güney, Plasmon Injection to Compensate and Control Losses in Negative Index Metamaterials, *Phys. Rev. Lett.* **115**, 035502 (2015).
- [28] H. Li, A. Mekawy, A. Krasnok, and A. Alù, Virtual Parity-Time Symmetry, *Phys. Rev. Lett.* **124**, 193901 (2020).
- [29] W. Adams, M. Sadatgol, X. Zhang, and D. Ö. Güney, Bringing the “perfect lens” into focus by near-perfect compensation of losses without gain media, *New J. Phys.* **18**, 125004 (2016).
- [30] X. Zhang, W. Adams, and D. Ö. Güney, Analytical description of inverse filter emulating the plasmon injection loss compensation scheme and implementation for ultrahigh-resolution hyperlens, *J. Opt. Soc. Am. B* **34**, 1310 (2017).
- [31] A. Ghoshroy, W. Adams, X. Zhang, and D. Ö. Güney, Active plasmon injection scheme for subdiffraction imaging with imperfect negative index flat lens, *J. Opt. Soc. Am. B* **34**, 1478 (2017).
- [32] W. Adams, A. Ghoshroy, and D. Ö. Güney, Plasmonic superlens imaging enhanced by incoherent active convolved illumination, *ACS Photonics* **5**, 1294 (2018).
- [33] A. Ghoshroy, W. Adams, X. Zhang, and D. Ö. Güney, Hyperbolic Metamaterial as a Tunable Near-Field Spatial Filter to Implement Active Plasmon-Injection Loss Compensation, *Phys. Rev. Appl.* **10**, 024018 (2018).
- [34] A. Ghoshroy, W. Adams, X. Zhang, and D. Ö. Güney, Enhanced superlens imaging with loss-compensating hyperbolic near-field spatial filter, *Opt. Lett.* **43**, 1810 (2018).
- [35] H. Wang, Y. Rivenson, Y. Jin, Z. Wei, R. Gao, H. Günaydin, L. A. Bentolila, C. Kural, and A. Ozcan, Deep learning enables cross-modality super-resolution in fluorescence microscopy, *Nat. Methods* **16**, 103 (2019).

- [36] I. J. Cox and C. J. R. Sheppard, Information capacity and resolution in an optical system, *J. Opt. Soc. Am. A* **3**, 1152 (1986).
- [37] Y. Katznelson, *An Introduction to Harmonic Analysis* (Dover Publications, New York, 1976).
- [38] M. C. Roggemann, D. W. Tyler, and M. F. Bilmont, Linear reconstruction of compensated images: Theory and experimental results, *Appl. Opt.* **31**, 7429 (1992).
- [39] W. H. Richardson, Bayesian-based iterative method of image restoration, *J. Opt. Soc. Am.* **62**, 55 (1972).
- [40] L. B. Lucy, An iterative technique for the rectification of observed distributions, *Astron. J. (NY)* **79**, 745 (1974).
- [41] L. Schermelleh, A. Ferrand, T. Huser, C. Eggeling, M. Sauer, O. Biehler, and G. P. C. Drummen, Super-resolution microscopy demystified, *Nat. Cell Biol.* **21**, 72 (2019).
- [42] P. Kner, B. B. Chhun, E. R. Griffis, L. Winoto, and M. G. L. Gustafsson, Super-resolution video microscopy of live cells by structured illumination, *Nat. Methods* **6**, 339 (2009).
- [43] A. G. York, S. H. Parekh, D. Dalle Nogare, R. S. Fischer, K. Temprine, M. Mione, A. B. Chitnis, C. A. Combs, and H. Shroff, Resolution doubling in live, multicellular organisms via multifocal structured illumination microscopy, *Nat. Methods* **9**, 749 (2012).
- [44] A. G. York, P. Chandris, D. Dalle Nogare, J. Head, P. Wawrzusin, R. S. Fischer, A. Chitnis, and H. Shroff, Instant super-resolution imaging in live cells and embryos via analog image processing, *Nat. Methods* **10**, 1122 (2013).
- [45] E. Wegel, A. Göhler, B. C. Lagerholm, A. Wainman, S. Uphoff, R. Kaufmann, and I. M. Dobbie, Imaging cellular structures in super-resolution with SIM, STED and localisation microscopy: A practical comparison, *Sci. Rep.* **6**, 27290 (2016).
- [46] F. Bottanelli, E. B. Kromann, E. S. Allgeyer, R. S. Erdmann, S. W. Baguley, G. Sirinakis, A. Schepartz, D. Baddeley, D. K. Toomre, J. E. Rothman, and J. Bewersdorf, Two-colour live-cell nanoscale imaging of intracellular targets, *Nat. Commun.* **7**, 10778 (2016).
- [47] S. A. Jones, S.-H. Shim, J. He, and X. Zhuang, Fast, three-dimensional super-resolution imaging of live cells, *Nat. Methods* **8**, 499 (2011).
- [48] H. Takakura, Y. Zhang, R. S. Erdmann, A. D. Thompson, Y. Lin, B. McNellis, F. Rivera-Molina, S.-N. Uno, M. Kamiya, Y. Urano, J. E. Rothman, J. Bewersdorf, A. Schepartz, and D. Toomre, Long time-lapse nanoscopy with spontaneously blinking membrane probes, *Nat. Biotechnol.* **35**, 773 (2017).
- [49] M. Bertero and P. Boccacci, Super-resolution in computational imaging, *Micron* **34**, 265 (2003).
- [50] Z.-p. Zeng, H. Xie, L. Chen, K. Zhanghao, K. Zhao, X.-s. Yang, and P. Xi, Computational methods in super-resolution microscopy, *Front. Inf. Technol. Electron. Eng.* **18**, 1222 (2017).
- [51] T. Hastie, R. Tibshirani, and J. Friedman, *The Elements of Statistical Learning* (Springer, 2016). <https://web.stanford.edu/~hastie/Papers/ESLII.pdf>.
- [52] W. Adams, C. Kendrick, C. T. Middlebrook, and D. O. Gunev, in *The 10th International Conference on Metamaterials, Photonic Crystals and Plasmonics* (2019), p. 511.
- [53] J. Miao, R. L. Sandberg, and C. Song, Coherent x-ray diffraction imaging, *IEEE J. Sel. Top. Quantum Electron.* **18**, 399 (2011).
- [54] Y. Zhang, T.-C. Poon, P. W. M. Tsang, R. Wang, and L. Wang, Review on feature extraction for 3-D incoherent image processing using optical scanning holography, *IEEE Trans. Ind. Informatics* **15**, 6146 (2019).
- [55] Y. J. Liu, B. Chen, E. R. Li, J. Y. Wang, A. Marcelli, S. W. Wilkins, H. Ming, Y. C. Tian, K. A. Nugent, P. P. Zhu, and Z. Y. Wu, Phase retrieval in x-ray imaging based on using structured illumination, *Phys. Rev. A* **78**, 023817 (2008).
- [56] P. Godard, M. Allain, V. Chamard, and J. Rodenburg, Noise models for low counting rate coherent diffraction imaging, *Opt. Express* **20**, 25914 (2012).
- [57] T. E. Gureyev, A. Kozlov, Y. I. Nesterets, D. M. Paganin, A. V. Martin, and H. M. Quiney, Signal-to-noise, spatial resolution and information capacity of coherent diffraction imaging, *IUCrJ* **5**, 716 (2018).
- [58] B. Chen, B. Abbey, R. Dilanian, E. Balaur, G. Van Riessen, M. Junker, C. Q. Tran, M. W. M. Jones, A. G. Peele, I. McNulty, D. J. Vine, C. T. Putkunz, H. M. Quiney, and K. A. Nugent, Diffraction imaging: The limits of partial coherence, *Phys. Rev. B* **86**, 235401 (2012).
- [59] G. J. Williams, H. M. Quiney, A. G. Peele, and K. A. Nugent, Coherent diffractive imaging and partial coherence, *Phys. Rev. B* **75**, 104102 (2007).
- [60] Y. Liu, Q. Liu, S. Zhao, W. Sun, B. Xu, and Z. He, Resolution enhancement in coherent diffraction imaging using high dynamic range image, *Photonics* **8**, 370 (2021).
- [61] P. Bhuvaneshwari and A. B. Therese, Edge detection techniques in digital and optical image processing, *Int. J. Eng. Res. Appl.* **4**, 33 (2014).
- [62] A. W. Lohmann and W. T. Rhodes, Two-pupil synthesis of optical transfer functions, *Appl. Opt.* **17**, 1141 (1978).
- [63] Y. Zhang, R. Wang, P. Tsang, and T.-C. Poon, Sectioning with edge extraction in optical incoherent imaging processing, *OSA Continuum* **3**, 698 (2020).
- [64] L. C. Andrews, *Laser Beam Propagation through Random Media* (SPIE, Bellingham, WA, 2005).
- [65] H. T. Eyyuboğlu, Y. Baykal, E. Sermetli, and Y. Cai, Scintillation advantages of lowest order Bessel-Gaussian beams, *Appl. Phys. B* **92**, 229 (2008).
- [66] M. E. Hanafy, M. C. Roggemann, and D. O. Gunev, Detailed effects of scattering and absorption by haze and aerosols in the atmosphere on the average point spread function of an imaging system, *J. Opt. Soc. Am. A* **31**, 1312 (2014).
- [67] M. E. Hanafy, M. C. Roggemann, and D. O. Gunev, Estimating the image spectrum signal-to-noise ratio for imaging through scattering media, *Opt. Eng.* **54**, 013102 (2015).
- [68] M. E. Hanafy, M. C. Roggemann, and D. O. Gunev, Reconstruction of images degraded by aerosol scattering and measurement noise, *Opt. Eng.* **54**, 033101 (2015).
- [69] H. Guerboukha, K. Nallappan, and M. Skorobogatiy, Toward real-time terahertz imaging, *Adv. Opt. Photonics* **10**, 843 (2018).
- [70] F. Monticone, C. A. Valagiannopoulos, and A. Alù, Parity-Time Symmetric Nonlocal Metasurfaces: All-Angle Negative Refraction and Volumetric Imaging, *Phys. Rev. X* **6**, 041018 (2016).

- [71] R. El-Ganainy, M. Khajavikhan, D. N. Christodoulides, and S. K. Ozdemir, The dawn of non-Hermitian optics, *Commun. Phys.* **2**, 37 (2019).
- [72] A. B. Mikhalychev, B. Bessire, I. L. Karuseichyk, A. A. Sakovich, M. Unternährer, D. A. Lyakhov, D. L. Michels, A. Stefanov, and D. Mogilevtsev, Efficiently reconstructing compound objects by quantum imaging with higher-order correlation functions, *Commun. Phys.* **2**, 134 (2019).
- [73] T. Gregory, P.-A. Moreau, E. Toninelli, and M. J. Padgett, Imaging through noise with quantum illumination, *Sci. Adv.* **6**, eaay2652 (2020).
- [74] G. H. Yuan, S. Vezzoli, C. Altuzarra, E. T. F. Rogers, C. Couteau, C. Soci, and N. I. Zheludev, Quantum super-oscillation of a single photon, *Light: Sci. Appl.* **5**, e16127 (2016).
- [75] G. Yuan, K. S. Rogers, E. T. F. Rogers, and N. I. Zheludev, Far-Field Superoscillatory Metamaterial Superlens, *Phys. Rev. Appl.* **11**, 064016 (2019).
- [76] T. Pu, J.-Y. Ou, N. Papasimakis, and N. I. Zheludev, Label-free deeply subwavelength optical microscopy, *Appl. Phys. Lett.* **116**, 131105 (2020).
- [77] G. Chen, Z.-Q. Wen, and C.-W. Qiu, Superoscillation: From physics to optical applications, *Light: Sci. Appl.* **8**, 56 (2019).
- [78] G. Di Francia, Directivity, super-gain and information, *IRE Trans. Antennas Propag.* **4**, 473 (1956).